ORIGINAL PAPER

Correlated conformational dynamics of the human GluN1-GluN2A type N-methyl-D-aspartate (NMDA) receptor

Sebnem Essiz[1] · Melis Gencel[1] · Muhammed Aktolun[1] · Ayhan Demir[1] · Timothy S. Carpenter[2] · Burak Servili[1]

Abstract

N-Methyl-D-aspartate receptors (NMDARs) are glutamate-gated ion channels found in the nerve cell membranes. As a result of overexcitation of NMDARs, neuronal death occurs and may lead to diseases such as epilepsy, stroke, Alzheimer's disease, and Parkinson's disease. In this study, human GluN1- GluN2A type NMDAR structure is modeled based on the X-ray structure of the *Xenopus laevis* template and missing loops are added by ab-initio loop modeling. The final structure is chosen according to two different model assessment scores. To be able to observe the structural changes upon ligand binding, glycine and glutamate molecules are docked into the corresponding binding sites of the receptor. Subsequently, molecular dynamics simulations of 1.3 µs are performed for both apo and ligand-bound structures. Structural parameters, which have been considered to show functionally important changes in previous NMDAR studies, are monitored as conformational rulers to understand the dynamics of the conformational changes. Moreover, principal component analysis (PCA) is performed for the equilibrated part of the simulations. From these analyses, the differences in between apo and ligand-bound simulations can be summarized as the following: The girdle right at the beginning of the pore loop, which connects M2 and M3 helices of the ion channel, partially opens. Ligands act like an adhesive for the ligand-binding domain (LBD) by keeping the bi-lobed structure together and consequently this is reflected to the overall dynamics of the protein as an increased correlation of the LBD with especially the amino-terminal domain (ATD) of the protein.

Keywords Ligand gated ion channels · Ionotropic glutamate receptors · Molecular dynamics · Principal component analysis · Homology and loop modeling

Introduction

N-Methyl-D-aspartate receptors (NMDARs) belong to the ionotropic glutamate receptor family (iGluR) along with the AMPA (α-amino-3-hydroxyl-5-methyl-4-isoxazole-propionate) and kainite receptors. They play a pivotal role in consciousness and standard memory and learning functions. iGluRs are all activated by glutamate and classified by

---

Melis Gencel and Muhammed Aktolun contributed equally to this work.

✉ Sebnem Essiz
  sebnem.gokhan@khas.edu.tr

[1] Bioinformatics and Genetics Department, Faculty of Engineering and Natural Sciences, Kadir Has University, 34083 Fatih, Istanbul, Turkey

[2] Biosciences and Biotechnology Division, Physical and Life Sciences Directorate, Lawrence Livermore National Laboratory, Livermore, CA, USA

additional specific agonists that bind them: AMPA, kainate, and NMDA (N-methyl-D-aspartate). Over-activation of iGluR is the leading cause of neurodegeneration and neural cell death, which are the causes of various types of dementia-related diseases such as Alzheimer's, Parkinson's, and Huntington's [1].

NMDARs are assembled from a pool of three different gene families: GluN1, GluN2 (A-D), and GluN3 (A-B) [2], and have at least one GluN1 subunit and two or more GluN2 or GluN3 subunits [3, 4]. Depending on receptor subunit composition, important functional characteristics like open channel conductivity and voltage dependence can vary [5]. NMDARs require glycine binding in GluN1 subunits and glutamate binding in GluN2 subunit for activation in membrane depolarization conditions.

Structurally, NMDARs are heterotetrameric proteins that consist of several regions: an extracellular amino-terminal domain (ATD), an extracellular ligand-binding site (LBD), a transmembrane domain (TMD), and an intracellular

carboxyl-terminal domain (CTD) [6, 7]. The clamshell-shaped ATD is composed of two lobes: upper (R1) and lower (R2). In the peptide chain topology, the ATD is followed by a sequence (S1) that forms the upper lobe (D1) of the clamshell-shaped LBD. S1 links the first (M1) of three transmembrane helices (M1, M3, and M4) to the LBD. A short linker connects M1 to M2 and a pore-lining reentrant loop (M2/p-loop) that generates the selectivity filter toward the interior of the channel. S2 sequence in LBD forms D2 lobe and hinge binding D2 to D1. Another short linker connects the M2/p-loop segment to the M3 helix of TMD (Fig. 1) [8].

Upon glutamate and glycine binding, the lower lobe (D2) of the clamshell comes close to the upper lobe (D1) and packs the ligand in the binding site. This motion pulls the pore-forming M3 helices in the TMD up, which leads to the opening and activation of the channel. This allows the passage of small cations including Na^+, K^+, and Ca^{2+}, but is blocked by Mg^{2+}, which is related to synaptic plasticity [9–11]. Other substances which are known to interact with NMDARs and modulate their activity include zinc cations, protons, polyamines such as dizocilpine (MK-801), and the psychotropic drug phencyclidine (PCP) [12].

In 2014, two X-ray structures gave insight into receptor structure arrangement and the inactive state of a full-length NMDAR [10, 13]. Until then, the only intact structure resolved by X-ray crystallography was for AMPA-GluR2 [14]. Additionally, several lower resolution cryo-EM structures of NMDAR captured inactivated and inhibited states as well as a triheteromeric structure, which has different subtypes [15–18].
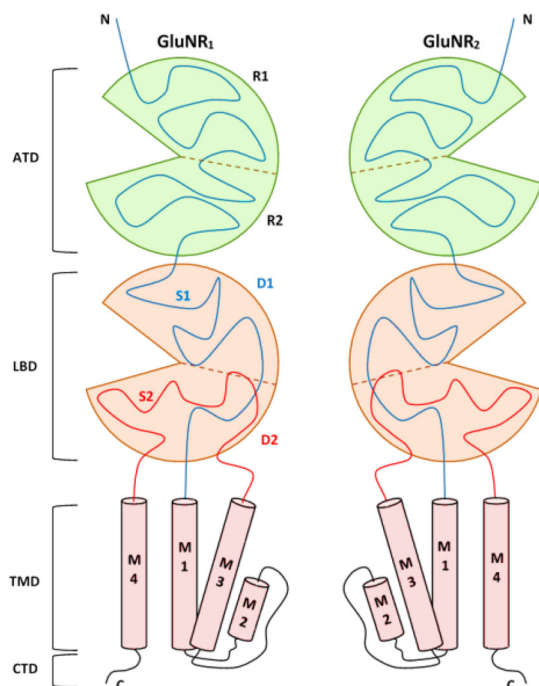

Fig. 1 Topology of NMDAR subunits

After the experimental structures became available, several computational studies are reported in the literature to address the structural transformations of the NMDAR structure. In one such study, the authors utilized targeted molecular dynamics (tMD), to model the open channel state of the receptor [19]. They started from the crystal structure for the inactivate state and forced the M3 helices to move toward the open channel model which is obtained based on correlation with SCAM, substituted cysteine accessibility method, data. In a similar study of Vasey et al., only the transmembrane segment of GluN1/GluN2A is modeled and refined by molecular dynamics (MD), and tMD with simulated annealing to study the dynamic behavior of the channel in the presence of divalent cations of Ca^{2+} and Mg^{2+} [20]. Mg^{2+} reduced the protein flexibility while Ca^{2+} binding showed similar fluctuations to no ion bound structure. Both studies used the AMPA receptor open channel conformation for the end state, however that structure is also not in open, but a pre-open state.

There are also recent MD studies on the human GluN1/GluN2B NMDAR homology models [21, 22]. One of these studies demonstrates that holo structure of NMDAR assumes a more tightly packed and stable conformation than the unbound NMDAR [21]. However, their simulation length is 300 ns, and they did not observe a fully-open ion channel structure. Additionally, they have different subtype model which included N2B. In another MD study, structures, which are determined under different experimental conditions, were mostly transformed into a structure similar to "desensitized" state of the channel [22].

In addition to MD studies, elastic network analysis has been carried out on the rat NMDA receptor structure. In this study, the activation is found to be carried out step by step through a series of structural motions from the ATD to inter and intrasubunit R2-D1 motions and to the LBD-M3 linkers to TMD [11]. An additional MD study investigated the inhibition mechanism of NMDAR ion channel blockers MK-801 and FDA approved drug memantine [23]. In this study, the protein was crystallized by cutting the ATD portion, and different symmetrical TMD/LBD was obtained in comparison to intact protein. This study demonstrated the importance of the ATD in stabilizing the structure in addition to its role as regulatory domain.

Despite the significant progress in structural studies of the NMDAR, the gating mechanism remains still elusive due to several reasons. The intact receptor structure that is open to ion transmission has not been experimentally resolved [24]. Furthermore, existing crystal structures include various mutations to reduce flexibility and enhance the quality of X-ray diffraction, such as disulfide crosslinks between subunits and the removal of certain resilient regions of the receptor, especially in the ion channel. The X-ray structures are also crystallized in the

presence of both partial agonists in LBD and allosteric inhibitors in ATD, which quite likely reflects the structure of a non-functional receptor [25].

In this work, the structure of GluN1-GluN2A type human NMDAR model was obtained via homology modeling method using X-ray structures which 4PE5 from *Rattus norvegicus* [10], and 4TLM from *Xenopus laevis* [13]. First, the two X-ray structures are compared in terms of loop structures and ion channel region resolutions. After picking the template and building the model, we performed total of 1.3 μs long MD simulations with two homology models, one with the ligand (holo) and the other one without ligand (apo) to see the effect of ligand binding on the structure and dynamics of the receptor.

Materials and methods

Homology modeling

The sequence identity of human GluN1 to frog GluN1, and human GluN2A to frog GluN2B (*Xenopus laevis*, PDB:4TLM) [10] is 92% and 81%, respectively while rat (*Rattus norvegicus*, PDB: 4PE5) NMDAR [13] showed about 98% sequence identity to human sequence for both chains. In the rat X-ray structure 15 charged residues are neutralized and 5 CYS cross-linking mutations have been introduced. Additionally, the M2-M1 linker region in the TMD is missing in the structure. A comparison of hole profiles between 4PE5 and 4TLM structures reveals that the frog X-ray structure is more detailed at the bottom of the gate area (Fig. S1). Consequently, the frog (4TLM) structure was chosen as a template in this work. Here, one might expect to use two templates together however addition of template(s) does not necessarily improve model quality [26, 27]. Here, we plan to utilize the information from the 4PE5 structure in the loop modeling step. Using ClustalW [28], the GluN1/GluN2A human sequences were aligned with the sequences of frog and rat, as well as the corresponding chains from AMPA and kainite receptors (Fig. S2 and Fig. S3). The resulting alignment of template sequences and human sequences were used in homology modeling by MODELLER [29, 30]. There are missing loop structures in both frog and rat structures. These main loops correspond to the three regions: the linker between the ATDs and LBDs, the linker between the LBDs and TMDs, (red highlighted segments in Fig. S2 and Fig. S3), and an intracellular loop (yellow highlighted in Fig. S3). In the homology modeling step by MODELLER, these segments are left out from modeling. The human structure is modeled as a tetramer based on the frog structure without the above-mentioned loop segments. One hundred models were generated and the best model was chosen using the DOPE [29, 30]

scoring function. The missing loops (except for the intracellular loop) in each chain were completed with Rosetta [31] kinematic closure loop modeling (red highlighted parts in Fig. S2 and Fig. S3). One hundred models are created for each loop, and the best loop combinations are picked by cross-checking in MODELLER and Rosetta scoring functions. Intracellular loop structure is not solved by any experimental studies, and it is too long to model. That is why it is left out of the scope of this study. Finally, the selected models are inspected with program PROCHECK [32] for stereochemical quality.

Ligand docking

The crystal structure reported by Lee et al. (PDB: 4TLM, frog) is in complex with the partial agonists 1-aminocyclopropane-1-carboxylic acid (ACPC) and trans-1-aminocyclobutane-1,3-dicarboxylic acid (t-ACBD) for GluN1 and GluN2B subunits, respectively) [10]. The structure also has GluN2B-specific allosteric inhibitor, Ro 25-6981, in the dimer interface between GluN1 and GluN2B ATDs. The other structure reported by Karakas et al. (PDB: 4PE5, rat) was crystallized with the GluN1 agonist, glycine, and the GluN2 agonist, L-glutamate, in the LBD and the allosteric inhibitor, ifenprodil, in the dimeric interface of GluN1/GluN2B ATDs [13].

When building the homology model, we used the frog structure (4TLM) by removing all the small molecules from the template structure. Then, the holo structure is obtained by docking the agonists glycine and glutamate into the LBDs of the model. Molecular docking of the glycine and glutamate to the model was performed using AutoDock4 [33]. The coordinates of ligands, glycine in GluN1 and glutamate in GluN2B subunits, were exported from the structure 4PE5. Glycine and glutamate molecules were positioned on the LBDs of GluN1 and GluN2A, respectively, by keeping the ligand structures flexible. Based on the crystal structure, the center for each ligand is selected from the LBD regions of each chain, and a grid box dimension is determined as $50 \times 50 \times 50$ Å. The number of docking runs was set to 100 in order to allow each ligand binds to the pockets in 100 different conformations. Docking experiments were carried out using a Lamarckian genetic algorithm with a maximum number of 2,500,000 energy evaluations for each ligand. The best 20 conformations are selected according to energy scores [34]. AutoDock4 is run for each chain and ligand with these parameters, and the best scored conformation of ligands is obtained for simulation.

Molecular dynamics

During the preparation of both models for MD simulations, the protonation states of histidine (HIS) and other charged residues (GLU, ASP, LYS, and ARG) have been determined

by the PROPKA [35] web server by calculating the pKa values of these residues at pH 7.4. Ligand-binding site aspartate residues are assigned to be in ionized states and all of the disulfide bridges between the close cysteine residues in the X-ray structure pdb files were applied to the system in VMD [36]. Both models were inserted into an unequilibrated palmitoyl-oleoyl phosphatidylcholine (POPC) membrane and solvated with TIP3P water molecules. Systems were neutralized by adding Na^+ and Cl^- ions into the system. At the end, systems consisting of nearly 230,000 atoms are obtained.

Two picoseconds (ps) (1000 steps) minimization and 2 nanosecond (ns) (1,000,000 steps) MD runs with 1 fs time step at a constant temperature of 310 K and at constant volume (NVT) were used for melting the lipid tails. The initial velocities were taken randomly from a Maxwellian distribution at 310 K. Then, both systems were simulated for 8 ns (four 2 ns simulation one after another with the spring constant 1, 0.75, 0.5, and 0.25 kcal/mol.$Å^2$, respectively) with positional constraints implemented on protein atoms at 310 K constant temperature and 1 atm constant pressure (NPT). The positional constraints on the protein atoms were completely removed and run for 5 ns (NPT, lipid area not constant) with constant system pressure (1 atm) and temperature (310 K) while all system atoms were released. Last, the lipid area was kept constant, and 1.3 μs in total were performed in a Langevin piston set to 1 atm for pressure and a Langevin temperature piston set to 310 K for temperature. All MD simulations were performed using NAMD [37] with a nonbonded vdW cutoff of 12 Å and the CHARMM [38] (v27 for lipid and protein) force field. Particle mesh Ewald electrostatics settings were applied, and the SHAKE algorithm was used for constrained hydrogen atoms. HOLE [39] was used to calculate the minimum pore radius along the ion channel. The last 1000 ns of the simulations were used for analysis.

PCA analysis

To analyze the collective conformational change of the systems, PCA is performed on the structures taken from MD simulations, using the PTRAJ [40] utility of AMBER [41]. Fifty thousand frames (1000 ns) were used. In the first step, each conformation in the trajectory was superimposed into the reference initial structure. In the second step, a variance-covariance matrix was constructed by calculating the deviations of positions from the average structure. The elements of the covariance matrix, C was calculated as:

$$C_{ij} = \, < x_i - \, < x_i >> . < x_j - \, < x_j >>$$

where x_i and x_j are the coordinates of C-alpha atoms of residues i and j, and the brackets means the ensemble average. The covariance matrix, C, can be decomposed as:

$$C = P \Delta P^T$$

where the eigenvectors, P, represent the principal components (PCs) and the eigenvalues are the elements of the diagonal matrix, Δ. Each eigenvalue is directly proportional to the variance it captures in its corresponding PC. Constructed matrix has $3\,N \times 3\,N$ dimension, N being the residue number. The eigenvectors represent the intrinsic collective motions of the protein and the corresponding eigenvalues, after removing 6 zero eigenvalues (3 for rotational and 3 for translational motions), represent the magnitudes of these motions [42]. To collect the collective motions and its magnitudes, normalized correlation matrices of the system are also calculated by the eigenvectors of the covariance matrix of 1000 ns long trajectory.

$$C_{ij} = \frac{\sum_{l=1}^{10} \dfrac{U_{il}U_{jl}}{\Omega_{ll}}}{\left(\sum_{m=1}^{10} \dfrac{U_{im}U_{jm}}{\Omega_{mm}}\right)^{\frac{1}{2}} \left(\sum_{n=1}^{10} \dfrac{U_{in}U_{jn}}{\Omega_{nn}}\right)^{\frac{1}{2}}}$$

where U is the matrix of eigenvectors, and Ω is the diagonal matrix of eigenvalues. The cross-correlations maps indicate correlation of motion between different parts of the protein.

Results

Model evaluation and docking

The percentage of amino acids present in the allowed "dihedral" angle combinations in the Ramachandran plots was 90% for the model and 94% for the template structure. The reason for rechecking the template structure, in addition to the homology models, is that the initial homology model quality is directly affected by the template quality. The models are constructed without loops, and were moved to a separate loop modeling step. There is a long intracellular loop structure which is missing in all X-ray structures and we also did not model that part.

ROSETTA [31] and MODELLER [29, 30] are used to reconstruct remaining missing loops and to compare the quality of results obtained. One such missing loop is between transmembrane helices M1 and M2 while the other is between ATD and LBD (Fig. S4A). From both programs, 100 different loop structures were collected for each missing loop. The reason why we built 100 loops in 2 different programs is to achieve better sampling for the loops, the two programs uses different algorithms for loop modeling. Then, all the loop structures were evaluated by using MODELLER's and ROSETTA's scoring functions (In Fig. S4B, the loops in $N1_1$ are displayed as an example). Both scoring functions

demonstrated better scores for loops modeled in ROSETTA. Then, the loops that have the highest Z-DOPE score were selected for the final homology model. Again, this cross-checking for the loop evaluation with two different programs provided us better sampling for the initial loop structures.

Before the simulation, the poses of the ligand molecules sorted by AutoDock results were also examined. For chain A, B, and C, the best scored pose of the ligand resembled the poses of glutamate and glycine in 4PE5 X-ray structure. However, in chain D, the best scored pose of the glutamate is rotated 180° in the binding pocket with respect to the pose in the X-ray structure. For that chain, we picked the second-best scored pose which is closer to the X-ray structure pose. The poses of initial glutamate and glycine in the holo structure and corresponding poses in the X-ray structure are provided in Supporting Fig. 5 (only chain C and D is shown for representative purposes).

MD simulation

The RMSD of the apo and holo simulations shows that the apo simulation seems to reach a plateau faster than the holo simulation, and both simulations reached a value of ~ 6 Å (Fig. 2). When individual domain RMSD values are checked, we observed ATD domain and ATD-LBD linkers have highest RMSD values while TMD is least mobile part of the complex. For both simulations, the first 300 ns is discarded and the remaining 1000 ns trajectory is used for the analysis.

The frog X-ray structure pore profile obtained in HOLE displays two restricted regions along the ion channel axis (Fig. S1C). The first girdle is across Thr 646 of GluN1 and Ala 645 of GluN2B, within the 'SYTANLAAF' motif. This girdle is considered the main gate of the channel at the boundary of M3 helices, also around TTTT gate [43]. The second girdle is close to the intracellular domain at the beginning of the pore loop which connects the M2 and M3 helices of the
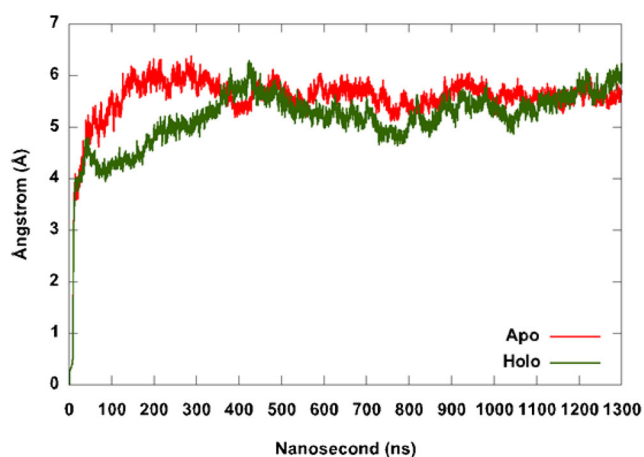
TMD. These two girdle regions are called top and bottom girdle consecutively in this work. The top girdle consists of the GluN1 of T648 and GluN2A of A647 and the bottom narrow region consists of the GluN1 of N616 and GluN2A of N614. The distances between the successive residues are measured and summed up for both top and bottom girdles during the production runs (Fig. 3a and Fig. 3b respectively). The top girdle distance (Fig. 3a) remained smaller in the apo simulation with a value around 31 Å while it is around 35 Å for the holo simulation (Fig. 3c). This 4 Å difference comes from the increase in one of the subunit pairs, distance between $GluN2A_2$ and $GluN1_1$. In Fig. 3e, the same distance is shown as distribution. The top girdle is sampling a more open structure in the holo simulation.

For the bottom girdle, the distance is 31 Å in apo simulation and 28 Å in holo simulation in the beginning (Fig. 3d). The distance remained almost constant for the apo simulation along the trajectory. However, a jump is observed for the holo simulation at around 220 ns to 38 Å. For the same distance, the holo simulation is sampling a wider range of values also (Fig. 3f). To investigate this brief opening at the bottom girdle, cross distance between the same residue pairs is also measured. The cross distance between $GluN1_1/GluN1_2$ stays larger (red lines in Fig. 4a), while $GluN2A_1/GluN2A_2$ decreases in holo when compared to apo simulations (green lines in Fig. 4a). In the bottom girdle, mainly GluN1 subunits move away from each other expand the channel. The conformational change of the bottom girdle is also inspected visually by selecting two frames from the trajectory (Fig. 4b and Fig. 4c). Tilt of M2 helix of $GluN1_1$ (Fig. 4b and Fig. 4c) pulls the pore-lining reentrant loop connected to M2 away from the pore. The M2 helix of $GluN2A_2$ rotates counterclockwise (Fig. 4b and Fig. 4c). These two subunits next to each other move away from the pore. Also, the M4 helices of the same subunits ($GluN1_1$ and $GluN2A_2$) slide to the left (Fig. 4c). In general, the brief opening in the bottom girdle is caused by neighboring subunits $GluN1_1$ and $GluN2A_2$ subunits.

Additionally, we checked the packing of the ATD and LBD domains during the trajectory. The distance between the center of masses of the ATD of each chain and the cross distances between the chains of LBD are displayed in Fig. 5a and Fig. 5b, respectively. The distances between the ATDs are ~ 203 Å in the apo simulation and ~ 194 Å in holo simulation (Fig. 5c). Thus, in the ligand-bound structure, the ATDs remain closer. This is consistent with a previous study by Tajima and coworkers in which they observed R2-R2 lobes of ATD are getting closer when the receptor is activated [15]. The LBD cross distances are ~ 65 Å and 75 Å for apo and holo simulation, respectively (Fig. 5d). Moreover, this distance fluctuates more in the holo simulation. The LBD ring stays more extended in the holo simulation, while the ATD subunits gets a more compact structure.

Fig. 2 The RMSD plot of apo and holo simulations. Apo (ligand-free) is represented by the red line, holo (ligand-bound) is represented by the green line

Fig. 3 **a** TMD top girdle. Selected residues are shown as red beads. **b** TMD bottom girdle. Selected residues are shown as green beads. **c** TMD Top girdle distances, shown in **a**, along the simulation. **d** TMD bottom girdle, shown in **b**, distances along the simulation. **e** TMD top girdle distance, shown in **a**, distribution. **f** TMD bottom girdle, shown in **b**, distance distribution
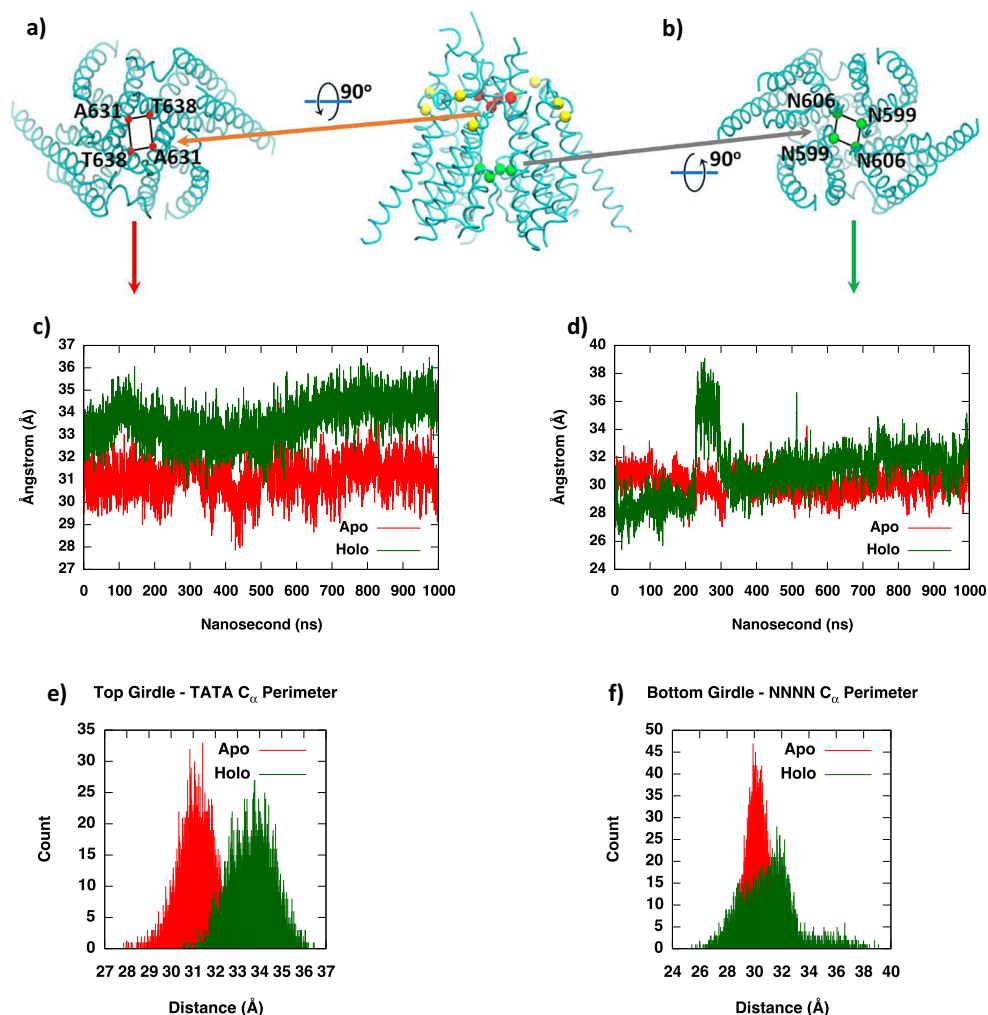
The LBD of each subunit contains two lobes (D1 and D2) connected via a hinge, and forms the agonist-binding cleft. The degree of closure of the two lobes is dependent on the agonist-binding affinity [10, 16]. The angle between the centroids of D1, D2, and the hinge point is displayed in Fig. 6a. The X-ray structure has partial agonists bound in the LBD. We removed those partial agonists and replace them with glycine and glutamate in our simulations. The initial angle in the X-ray structure is ~ 101° for GluN1 and ~ 143° for GluN2 subunits. This angle stays around the same value for the GluN1$_1$, GluN1$_2$, and GluN2A$_1$ subunits. The angle in the GluN2A$_2$ subunit is larger (~ 115°) in both simulations when compared with the rest of the subunits. Additionally, in GluN2A$_2$, the holo simulation has a hinge angle ~ 5° smaller with respect to apo.

The distances between the center of mass (COM) of the R2 lobe of the ATD and the COM of the D1 lobe of the LBD are monitored to observe the inter-domain separation (Fig. 6b). The distances between ATD/LBD of the both GluN1 subunits are larger in the apo simulation with respect holo. For GluN2A subunits, a lower distance is observed in the apo simulation relative to

holo. Also, for the second GluN2A subunit, the distance gets as small as 28 Å. The two subunits distances behaved differently.

The lengths of linkers connecting the LBD to the TMD are displayed in Fig. 7. The M3/S2 linker is the connection between D2 of the LBD and M3 of the TMD. The M3/S2 linker of GluN1 is vertical to the membrane, and the M3/S2 linker of GluN2A is parallel to membrane (Fig. 7a). This linker is almost 12 Å longer for GluN2A subunits in holo simulation. No significant difference was observed for the GluN1 M3/S2 loops (Fig. 7b). In the study by Twomey et al. 2017 [44], the M3/S2 linker was measured to determine the differences of chains in ion channel opening behavior and it has been shown that only M3/S2 linkers parallel to the membrane play a central role in gating. Also, in the cryo-EM structures of the triheteromeric NMDA receptor, the N2A subunit ATD resides on top of LBD, and participates in extensive interactions with LBD when compared with the N2B subunits [17]. In our simulations also, N2A displayed a different behavior in terms of the linker region.

Fig. 4 **a** TMD bottom girdle cross distances. **b**, **c** Alignment of the narrowest (Hologray) and widest (Holo-light gray) states of the bottom gate. **b** Bottom view of the channel. M3 and M2 helices displayed opaque, M4 and M1 helices are transparent. **c** Side view of the channel. M2 and M4 helices materialized as opaque and M1 and M3 helices did not showed
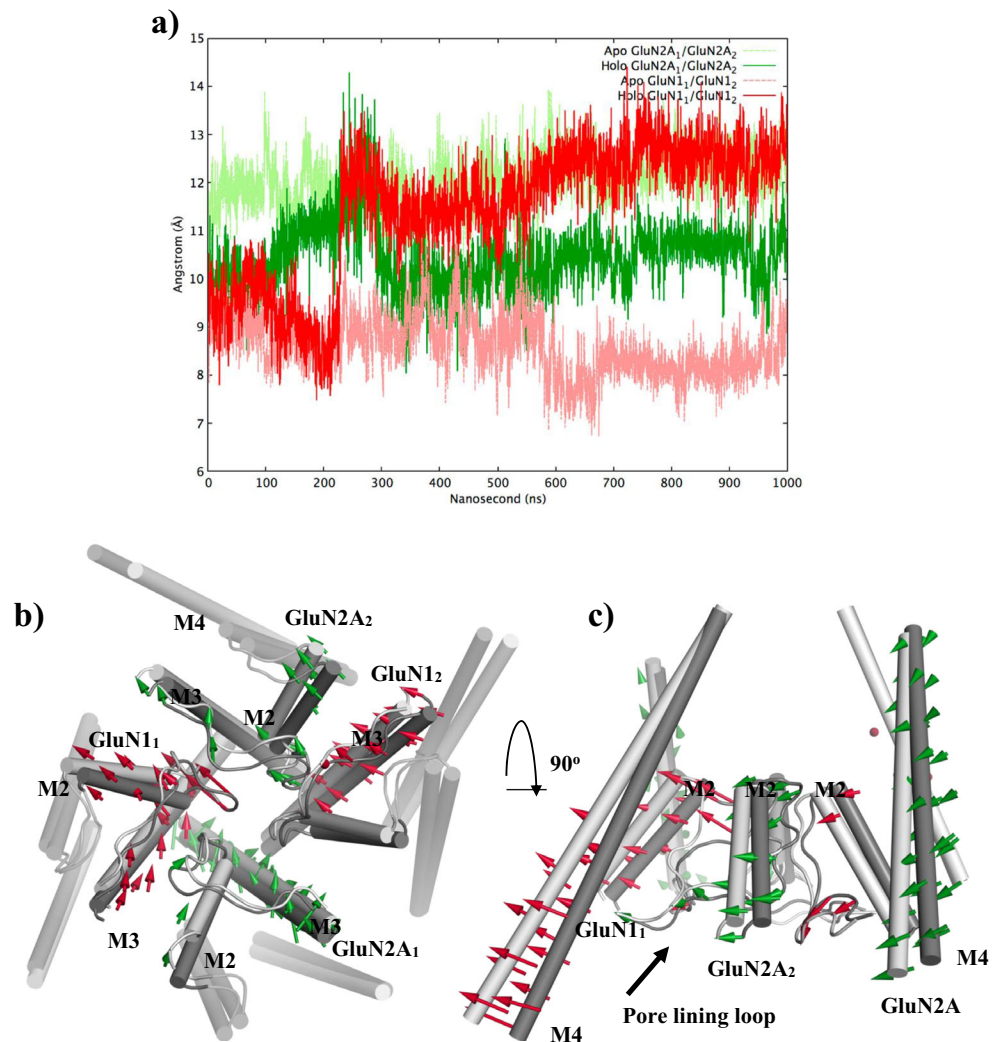
Effect of agonist and co-agonist binding on intrinsic dynamics

PCA is performed for the 1000 ns (50,000 frames) equilibrated trajectory of apo and holo simulations. Previous studies have shown that the first 10 eigenvalues are sufficient to capture most of the fluctuations in the protein [45, 46]. In this study, the first 10 eigenvalues cover 65% of total fluctuations in the apo simulation and 77% of total fluctuations in the holo simulation. The largest amplitude motion of the protein is represented by the first eigenvalue. Fluctuations of the first mode of the holo simulation are almost two times higher than apo. The first mode of the holo covers 48.1% of the total movement of the protein, while in the apo simulation, the same mode covers 28.8%.

Figure 8 displays the mode with the largest variance value (first eigenvector) for different subunits. The ATD and the LBD are more mobile in both simulations compared to the TMD. This mode exhibits similar motions for apo and holo simulation but with very different amplitudes.

More "collective and concerted" movements are observed in the holo simulation, and the amplitudes of motion are larger. In the holo simulation, the rotation of the LBD region as a rigid body upon ligand binding promotes the upward motion of the helices along the membrane axis. This motion is most obvious for GluN2A$_1$ subunit (purple subunits in Fig. 8b). The ATD subunit is rotating as a rigid body, while the LBDs and TMD seems rotating in opposite direction to the ATD. This motion is similar to the proposed AMPA gating mechanism [44] in which LBD cleft closure pulls the linkers to open the channel pore. In GluN2A subunits, R2 of ATD moves away from the center of ATD, and R1 of ATD gets close to channel tunnel. While for dimers of GluN1, R2 of ATD rotates counterclockwise and approaches the LBD. In both systems, TMD mobility was lower compared to the extracellular part of the protein.

Moreover, the relative rotation of the different domains is calculated by the hingefind algorithm [47] (Fig. 9). First, we checked the differences only in ATD domain. This domain is observed to show bending along this axis in previous cryo-
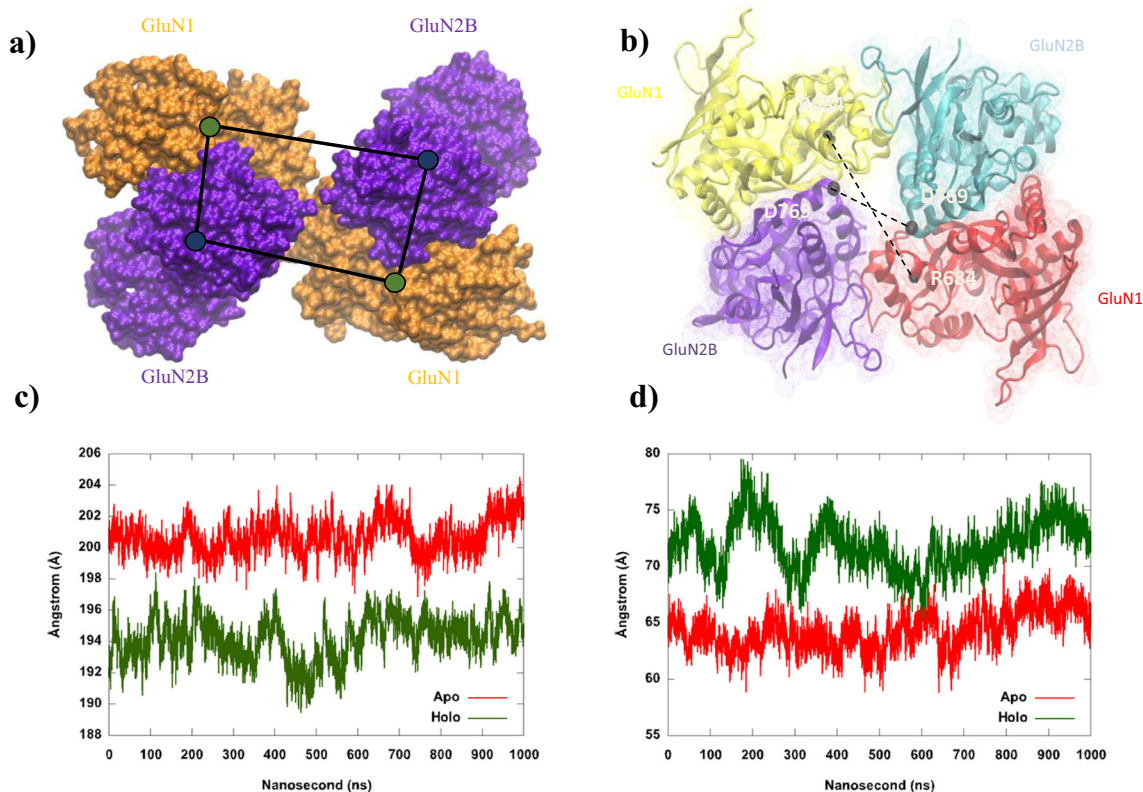
Fig. 5 a ATDs are shown as surface representation in orange for GluN1 and purple for GluN2A. Circles show the center of masses of each domain in same color codes and the black rods represent the measured distances. **b** LBDs are shown as cartoon representation with the color codes yellow and red for GluN1, cyan and purple for GluN2A. Residues selected are shown as black spheres and dashed lines show the distances measured. Distance graphs for the apo and ligand-bound trajectories are shown under each of the corresponding parameters

EM structures [16]. To observe the rotation of ATD only, the TMD and LBDs are kept as a rigid body. The rotation angles are displayed in Table 1. In general, the ATD rotation angle for each subunit is larger in the ligand-bound structure (5° to 17° more rotation), and the ATD of GluN2A$_1$ show the largest rotation angle. When only TMD subunit is taken as a rigid body to observe the rotation movement of extracellular domain (LBDs and ATDs) as a single unit, again the holo structure shows larger rotation values. Again, one of the GluN2A subunits, GluN2A$_2$ displays the biggest difference from apo structure with an increase in angle of 9°.

Cross-correlation graphs are obtained from normalized covariance matrix values based on C atoms (Fig. 10). In the correlation graphs, the diagonal regions are for spatially proximal parts of the protein, while the off-diagonal regions indicate the correlation between the distal parts.

According to the cross-correlation map of GluN1$_1$ (Fig. 10a), S2 and S1 domains in the LBD display higher correlated motion with R2 lobe of ATD in the holo simulation. S1 is the sequence connecting the LBD to M1 helix of the TMD, and S2 is the sequence connecting M3 to M4 helix in the TMD. Also, these R1 and R2 parts of the cross-correlation map indicate that the R2 lobe of the ATD and the D1 lobe of the LBD move together. The S1 and S2 domains include D1

and D2 lobes and hinge regions in LBD. Another significant change is that the R1 lobe of the ATD displays correlated motion with the M1/M3 helices upon ligand binding. Hence, M4 and M3 helices of GluN1$_1$ display greater correlation in the holo simulation. So, in this subunit, the lower ATD lobe R2 shows correlated motions with the LBD and TMD, the R1 upper lobe of ATD shows anti-correlated behavior.

The major differences in the correlated motions for GluN2A$_1$ (Fig. 10b) are observed as the following: S1 with S2 regions in the LBD, R2 lobe of ATD with S1 of LBD, M1/M3 helices of TMD with R1 of ATD, and the M4 helices with M1/M3 helices. In these regions, the correlation is greater in the holo simulations. Additionally, there is anti-correlated motion between ATD and LBD in holo simulation (blue regions).

For GluN1$_2$ and GluN2A$_2$ (Fig. 10c and Fig. 10d) again the S1 and S2 regions of the LBDs showed a higher correlation in the holo simulation compared to apo, similarly to the GluN2A$_1$ chain. Upon ligand binding, R1 of the ATD and the LBDs show anti-correlated motion in GluN1$_2$, while in GluN2A$_2$, the same regions show correlated motions (Fig. 10d). There are correlated movements between M1/M3 helices and the ATD for both GluN1$_2$ and GluN2A$_2$.

In summary, the S1 and S2 regions of the LBD show a higher correlation in the holo simulation, indicating that ligand
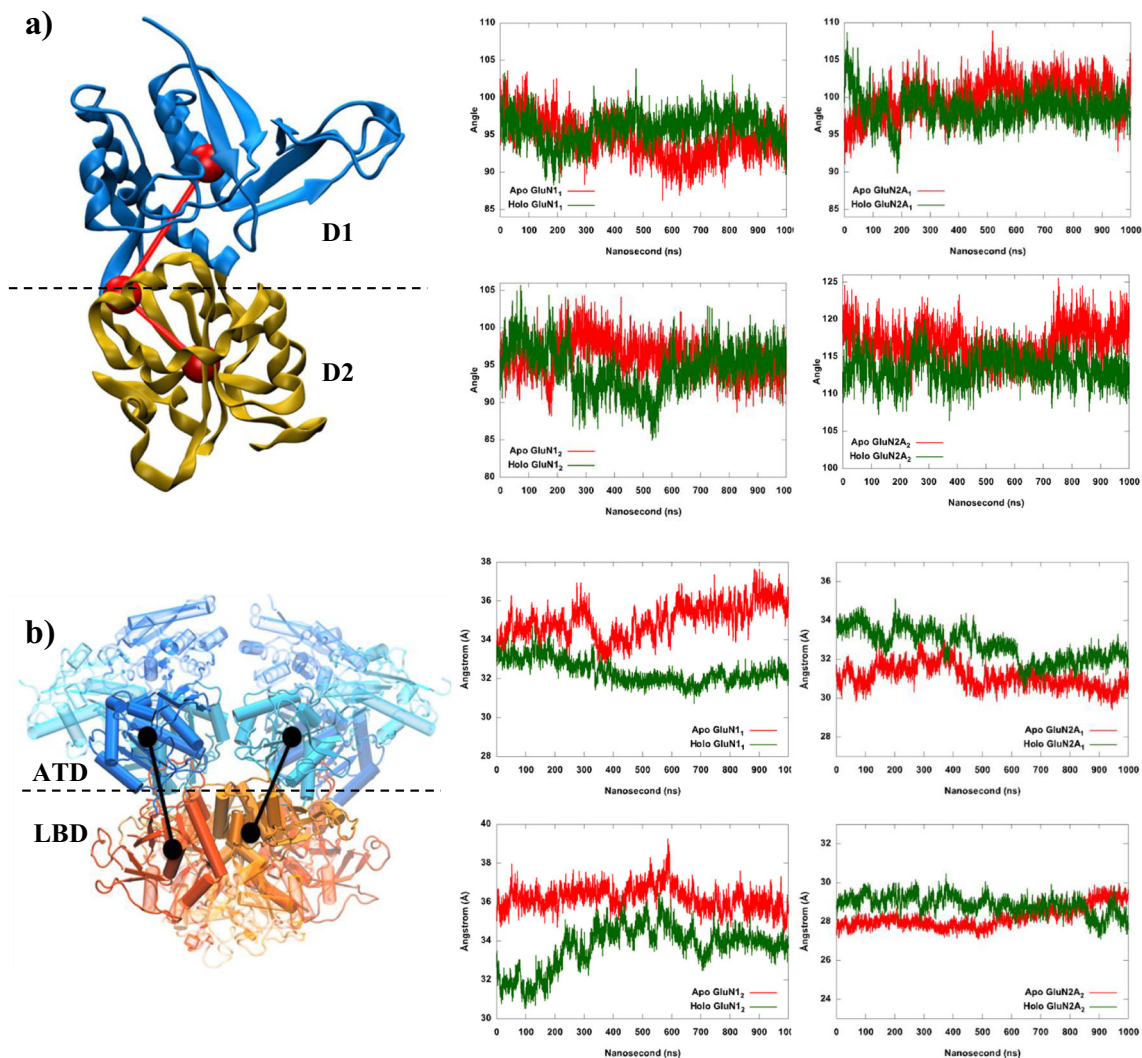
Fig. 6 Intra/inter-domain movement analysis of LBD. **a** Visual representation of LBD clamshell. Blue color represents D1 lobe and yellow color represents D2 lobe of LBD. Red balls are COM of D1, D2 and hinge part. Red line are the vectors that connects to COMs. Graphs: This angle is plotted for each subunit along the trajectory (Red line apo, green line holo simulations). **b** Visual representation of ATD/LBD. R1 and D2 lobes are shown with transparent and R2 and D1 lobes are shown with opaque colors. Black spheres are the COMs of R2 and D1 lobes and black line shows the measured distance. ATD is represented with blue color while LBD is represented with orange color. Darker color represents GluN1 subunits and lighter colors represent GluN2A subunits. Graphs: The distance is plotted for each subunit along the trajectory (Red line apo, green line holo simulations)

molecules bring these two segments together and then they move in more correlated fashion in holo simulations. Another observation is that the correlation between the distant domain ATD and the M1/M3 helices of TMD increases upon ligand binding. In all chains, the correlation between the LBD and the ATD is increased when the ligand is bound in the LBD region. Lastly, increased correlations are occurred between the M4 helix and the M1/M3 helices for each subunit. Ligand binding induces a conformational change that increases both the intra- and inter-domain coupling.

In Fig. 11, RMSF are plotted for each subunit. Region 1 is a loop in R1 lobe of ATD while.

Region 2 is the linker region that connects R2 lobe of ATD to LBD. These loops showed higher deviations over

course of holo simulation (Fig. 10a). Region 3, the hinge region in ATD in GluN2A$_1$, showed higher fluctuation in holo compared apo. Also, S1 and S2 sequences in LBD display higher flexibility (Region 4 and Region 6) in GluN2A$_1$. Another increase in deviation is observed at the TMD part (Region 5) (Fig. 11b). In GluN1$_2$, there are two region that showed higher fluctuations in holo simulation. Region 7 is a loop that located at D1 lobe of LBD. Region 8 is the linker that connects to LBD to M4 helix which showed a noticeable flexibility (Fig. 11c). R2 lobe of ATD and linker that connect to ATD to LBD demonstrate higher mobility for GluN2A$_2$ (Fig. 11d). Overall, the loops and the linkers that connect the lobes or the domains displayed large peaks in both structures.

Fig. 7 Distance change of M3/S2 linker between subunits. M3/S2 link connects the M3 helix to D2 of LBD. **a** The cartoon representation of linkers. **b** The distance change of linker between subunits is plotted. Dashed line represents GluN1 subunit and straight line represents GluN2A subunits. Apo simulation is represented with red, holo simulation represented with green
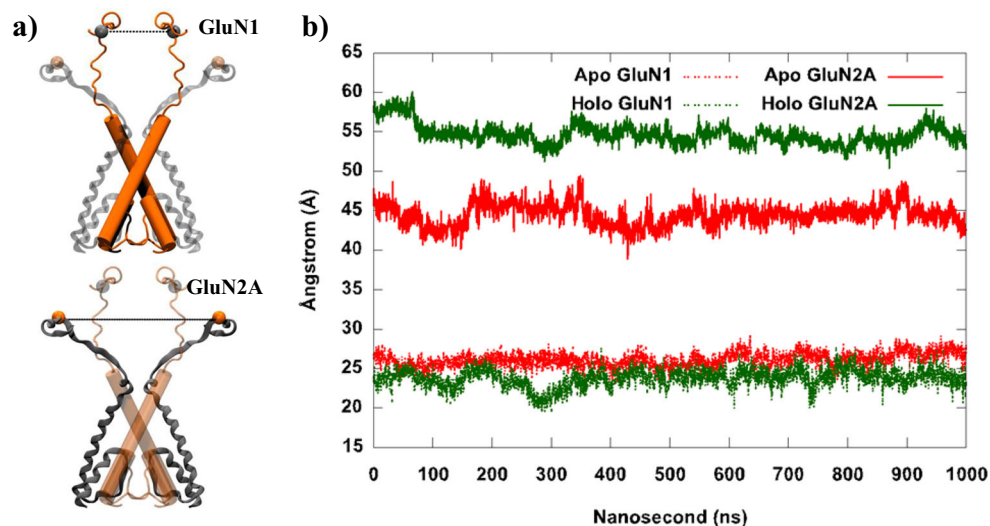
Discussion

First, we analyzed structural changes of the receptor with parameters that are adopted from X-ray structural studies [10, 13]. The ATD becomes more compact after ligand binding, and R1/R2 lobe opening is observed for GluN2A$_2$ subunits. Previous studies suggest that R1 and R2 rearrange themselves to open after ligand binding. In addition, in the holo structure, the LBD ring expanded through the GluN1 subunits. We also observed a larger distance between the ATD and LBD in GluN2A subunits upon ligand binding.

The main difference in the D1/D2 angle is also observed for GluN2A subunit. Consecutively, the linker region between the LBD and TMD becomes longer in the holo simulation.

Mainly the change in angle between the D1/D2 lobes pulls the LBD and ATD closer, and this results as longer loops in the TMD/LBD interface. This mechanism is similar to the current view of activation in this receptor, in which the conformational change of the LBD and ATD cleft closure is propagated to the transmembrane segments by pulling M3 helices by the M3/S2 linker, thereby leading to receptor activation and subsequent desensitization [48].

Overall GluN2A subunits displayed a more significant conformational change with respect to GluN1 subunits in this study. Especially the linker M3/S2 is almost 12 Å longer for GluN2A subunits in holo simulation while there is no significant difference in GluN1. This type of conformational difference in between different subunits or chains is also detected in

Fig. 8 First mode representations of both simulation. **a** GluN1$_1$ were represented with an orange color and GluN1$_2$ were represented with blue. **b** GluN2A$_1$ were represented with purple color and GluN2A$_2$ were represented with green
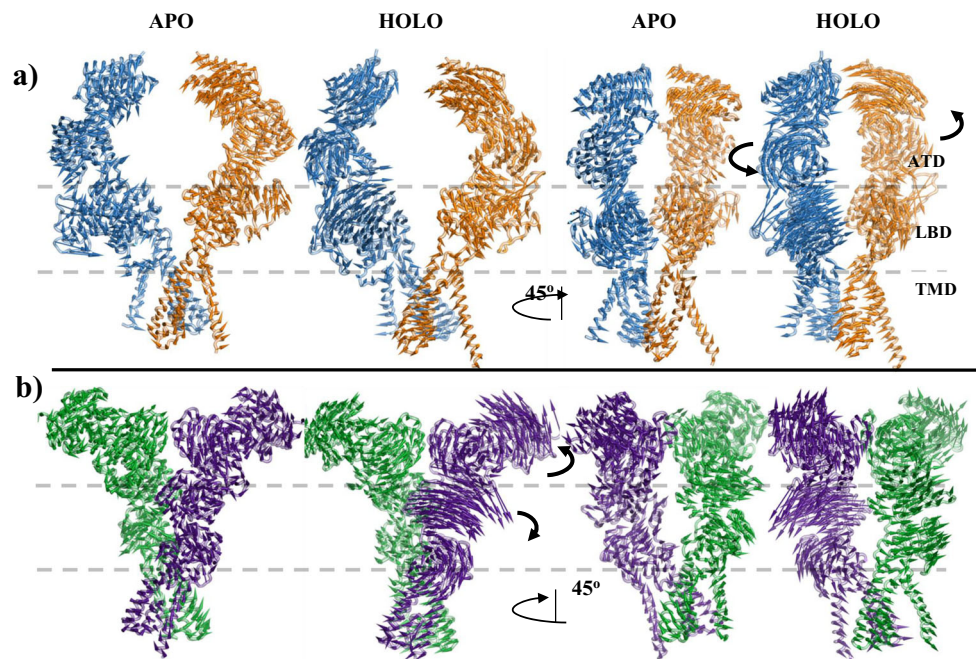
Table 1 Rotation angles

	ATD rotation (°)				Extracellular domain rotation (ATD and LBD together) (°)			
	$GluN1_1$	$GluN2A_1$	$GluN1_2$	$GluN2A_2$	$GluN1_1$	$GluN2A_1$	$GluN1_2$	$GluN2A_2$
Apo	7	6	8	1	3	2	5	5
Holo	12	23	13	11	5	5	7	14

previous studies [19, 49–55]. Namely GluN1 and GluN2A are responding to ligand binding differently.

In the TMD region, both top and bottom girdle remained wider in the holo simulation. For a brief 100 ns, the bottom girdle was opened. During this opening, the M2 helices of $GluN1_1$ and $GluN2A_2$ move outwards from channel. These subunits are adjacent, so the opening is not from symmetric subunits. In the original X-ray structures, the TMD had segments missing in the electron density [10, 13]. Namely, the rat structure does not have the bottom girdle fully resolved. Thus, it is possible that in the simulations, we might be observing the effect of these regions coming to an equilibrium state in addition to the effect of the ligand.

The TMD of the NMDARs is similar in structure to the voltage gated K+ channel. However, in the voltage gated the potassium channels such as KscA, there is a highly charged intracellular region of channels which contribute to the channel opening by the changes in the local electrostatic changes. NMDARs are like upside down of these voltage gated K+ channels with the same conserved helix bundle crossing. However, they lack this highly charged voltage sensor regions. Thus, instead of these voltage sensors, the changes in the conformation of LBD upon ligand binding cause a pulling

action on the TMD through the M3/S2 linkers [56]. We also observe the same pulling from this linker region on the top of TMD.

Correlation map analyses showed that there is an increase in correlation between the ATD and the TMD M1/M3 helices after ligand binding. Also, R1 of the ATD showed anti-correlation with the LBD for every subunit except $GluN2A_2$ chain. Correlation increased between the M4 helix and M1/M3 of the TMD for every subunit after ligand binding. Mainly ligand binding holds the D1 and D2 lobes of the LBD together and results in a higher correlation between the ATD and TMD.

The PCA analysis displayed results in which the whole ECD or ATD rotation is larger in the holo simulation. Again, the largest rotation angles are observed for GluN2A subunits. This whole ECD rotation is detected in the cryo-EM structures of six distinct classes of density maps of the GluN1-GluN2B NMDAR [16].

Overall, the X-ray structures that are used in this analysis had partial agonist in the LBD, and allosteric inhibitors in ATD, which quite likely reflects the structure of a non-functional receptor. Additionally, due to the introduction of cross-linking and mutations into these structures may result in
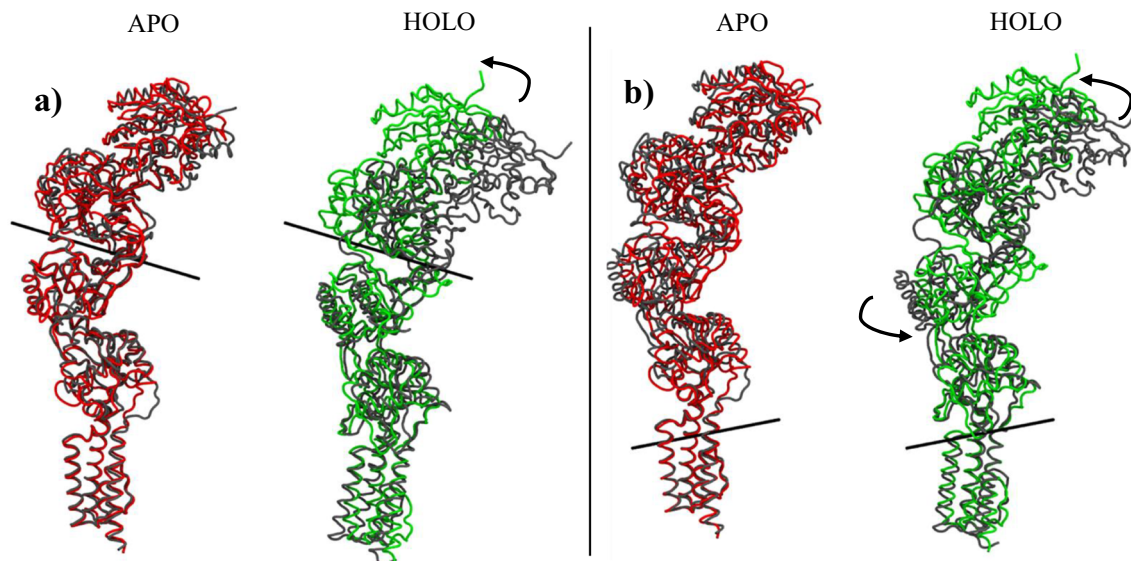

Fig. 9 The rotation angles in the PCA first mode. **a** The representation of ATD rotation between two conformations from first mode of PCA. Black rods show the rotation axis. Green represent holo red represent apo structure modes. **b** The representation of ATD/LBD rotation rotation between two conformations from first mode of PCA. Black rods show the rotation axis. Green represent holo red represent apo structure modes

Fig. 10 Correlation plots of apo (lower right half-matrix) and holo (upper left half-matrix) for different subunits
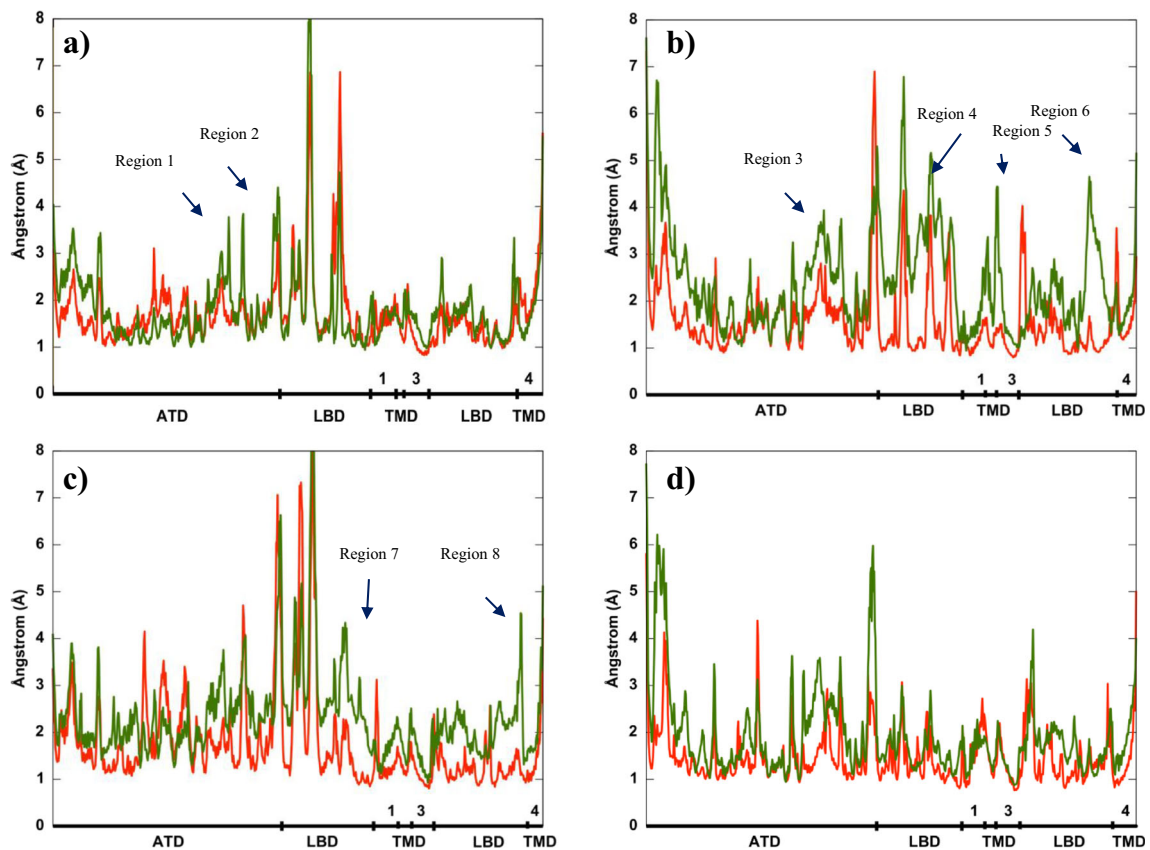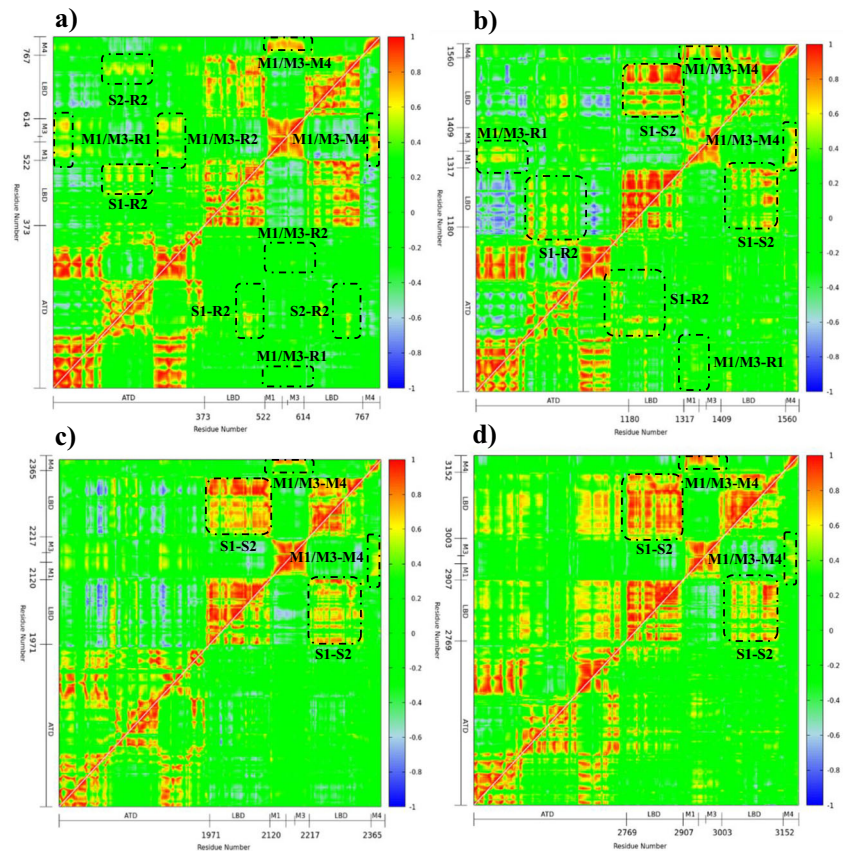

Fig. 11 Root-mean-square fluctuations (RMSF) graphs of (**a**) GluN1$_1$, (**b**) GluN2A$_1$; (**c**) GluN1$_2$, and (**d**) GluN2A$_2$ subunits of apo (red) and holo (green) simulations

a non-functional state. All these corrections are introduced into the modeling step very carefully and equilibrated through 1300 ns simulations only when glycine and glutamate are bound in LBD. Thus, we did not expect to see a full change in the functional state of the protein that would not be realistic with these many uncertainties in the initial structure although the simulation length is relatively long. In this study, our aim is to study the differences in the equilibrium dynamics of the receptor when ligand is bound in LBD site and presenting as simple picture as possible without too many contradicting effects such as having both agonist in LBD and inhibitor in ATD at the same time. As a result, we mainly observed more correlated dynamics of LBD with the other two domains. Also, more rigid body rotations in LBD are reflected to ion channel helices with the elongation of linker regions in holo simulations. The mobility of LBD and ATD with respect to TMD region is much more visible in the holo simulations. This type of mobility of the extracellular domain is also observed in cryo-EM images [16]. The correlation of the motions of ATD and LBD are also found to be significantly increased when ligand is present. This finding is along the line of the regulatory behavior of ATD characteristic to only NMDA type receptors in the iGluR family.

Last but not least, negative cooperativity of glycine and glutamate is also well known with NMDAR, i.e., receptor's affinity for glycine being lowered upon binding glutamate [48]. Here, we have both type of ligands bound on LBD simultaneously, but still GluN2A chains which have glutamate in the binding site displayed higher correlations and larger amplitude motions compared to GluN1 which has glycine in the binding site. We hope the findings of this study especially the different behavior of subtypes in the allosteric mechanism will be further tested when full-length structures of NMDARs with only one type of agonist bound becomes available.

Author contribution Conceived and designed the experiments: Sebnem Essiz, Melis Gencel, and Muhammed Aktolun. Performed the experiments: Melis Gencel, Muhammed Aktoulun, Ayhan Demir. Analyzed the data: Sebnem Essiz, Melis Gencel, Muhammed Aktolun, Burak Servili, and Timothy S. Carpenter. Wrote the paper: Sebnem Essiz and Melis Gencel.

Declarations

Conflict of interest The authors declare no competing interests.

References

1. Gillessen T, Budd SL, Lipton SA (2002) Excitatory amino acid neurotoxicity. Adv Exp Med Biol 513:3–40
2. Dingledine R et al (1999) The glutamate receptor ion channels. Pharmacol Rev 51(1):7–61
3. Kuryatov A et al (1994) Mutational analysis of the glycine-binding site of the NMDA receptor: structural similarity with bacterial amino acid-binding proteins. Neuron 12(6):1291–1300
4. Ozawa S, Kamiya H, Tsuzuki K (1998) Glutamate receptors in the mammalian central nervous system. Prog Neurobiol 54(5):581–618
5. Gillessen T, Grasshoff C, Szinicz L (2002) Mitochondrial permeability transition can be directly monitored in living neurons. Biomed Pharmacother 56(4):186–193
6. Laube B, Kuhse J, Betz H (1998) Evidence for a tetrameric structure of recombinant NMDA receptors. J Neurosci 18(8):2954–2961
7. Rosenmund C, Stern-Bach Y, Stevens CF (1998) The tetrameric structure of a glutamate receptor channel. Science 280(5369):1596–1599
8. Ryan TJ et al (2008) Evolution of NMDA receptor cytoplasmic interaction domains: implications for organisation of synaptic signalling complexes. BMC Neurosci 9:6
9. Schneggenburger R et al (1993) Fractional contribution of calcium to the cation current through glutamate receptor channels. Neuron 11(1):133–143
10. Lee CH et al (2014) NMDA receptor structures reveal subunit arrangement and pore architecture. Nature 511(7508):191–197
11. Zheng W et al (2017) Probing the structural dynamics of the NMDA receptor activation by coarse-grained modeling. Biophys J 112(12):2589–2601
12. Ransom RW, Stec NL (1988) Cooperative modulation of [3H]MK-801 binding to the N-methyl-D-aspartate receptor-ion channel complex by L-glutamate, glycine, and polyamines. J Neurochem 51(3):830–836
13. Karakas E, Furukawa H (2014) Crystal structure of a heterotetrameric NMDA receptor ion channel. Science 344(6187):992–997
14. Sobolevsky AI, Rosconi MP, Gouaux E (2009) X-ray structure, symmetry and mechanism of an AMPA-subtype glutamate receptor. Nature 462(7274):745–756
15. Tajima N et al (2016) Activation of NMDA receptors and the mechanism of inhibition by ifenprodil. Nature 534(7605):63–68
16. Zhu S et al (2016) Mechanism of NMDA Receptor inhibition and activation. Cell 165(3):704–714
17. Lu W et al (2017) *Cryo-EM structures of the triheteromeric NMDA receptor and its allosteric modulation.* Science **355**(6331)
18. Stroebel D, Casado M, Paoletti P (2018) Triheteromeric NMDA receptors: from structure to synaptic physiology. Curr Opin Physiol 2:1–12

19. Pang X, Zhou HX (2017) Structural modeling for the open state of an NMDA receptor. J Struct Biol 200(3):369–375

20. Mesbahi-Vasey S et al (2017) All atom NMDA receptor transmembrane domain model development and simulations in lipid bilayers and water. PLoS One 12(6):e0177686

21. Palmai Z et al (2018) How does binding of agonist ligands control intrinsic molecular dynamics in human NMDA receptors? PLoS One 13(8):e0201234

22. Sinitskiy AV, Pande VS (2018) Computer simulations predict high structural heterogeneity of functional state of NMDA receptors. Biophys J 115(5):841–852

23. Song X et al (2018) Mechanism of NMDA receptor channel block by MK-801 and memantine. Nature 556(7702):515–519

24. Schmid SM, Hollmann M (2008) To gate or not to gate: are the delta subunits in the glutamate receptor family functional ion channels? Mol Neurobiol 37(2–3):126–141

25. Cerny J et al (2019) NMDA receptor opening *and closing-transitions of a molecular machine revealed by molecular dynamics*. Biomolecules **9**(10)

26. Chakravarty S, Godbole S, Zhang B, Berger S, Sanchez R (2008) Systematic analysis of the effect of multiple templates on the accuracy of comparative models of protein structure. BMC Struct Biol 8 (1):31

27. Ayan M, Essiz S (2018) The neural $\gamma2\alpha1\beta2\alpha1\beta2$ gamma amino butyric acid ion channel receptor: structural analysis of the effects of the ivermectin molecule and disulfide bridges. J Mol Model 24 (8):207

28. Thompson JD, Higgins DG, Gibson TJ (1994) CLUSTAL W: improving the sensitivity of progressive multiple sequence alignment through sequence weighting, position-specific gap penalties and weight matrix choice. Nucleic Acids Res 22(22):4673–4680

29. Fiser A, Sali A (2003) Modeller: generation and refinement of homology-based protein structure models. Methods Enzymol 374:461–491

30. Marti-Renom MA et al (2000) Comparative protein structure modeling of genes and genomes. Annu Rev Biophys Biomol Struct 29:291–325

31. Rohl CA et al (2004) Modeling structurally variable regions in homologous proteins with rosetta. Proteins 55(3):656–677

32. Laskowski RA et al (1993) PROCHECK: a program to check the stereochemical quality of protein structures. J Appl Crystallogr 26(2):283–291

33. Morris GM et al (2009) AutoDock4 and AutoDockTools4: automated docking with selective receptor flexibility. J Comput Chem 30(16):2785–2791

34. Huey R et al (2007) A semiempirical free energy force field with charge-based desolvation. J Comput Chem 28(6):1145–1152

35. Olsson MH et al (2011) PROPKA3: consistent treatment of internal and surface residues in empirical pKa predictions. J Chem Theory Comput 7(2):525–537

36. Humphrey W, Dalke A, Schulten K (1996) VMD: visual molecular dynamics. J Mol Graph 14(1):33–38

37. Phillips JC et al (2005) Scalable molecular dynamics with NAMD. J Comput Chem 26(16):1781–1802

38. Feller SE, MacKerell AD (2000) An improved empirical potential energy function for molecular simulations of phospholipids. J Phys Chem B 104(31):7510–7515

39. Smart OS et al (1996) HOLE: a program for the analysis of the pore dimensions of ion channel structural models. J Mol Graph 14(6):354–360

40. Roe DR, Cheatham 3rd TE (2013) PTRAJ and CPPTRAJ: software for processing and analysis of molecular dynamics trajectory data. J Chem Theory Comput 9(7):3084–3095

41. Case DA et al (2005) The Amber biomolecular simulation programs. J Comput Chem 26(16):1668–1688

42. David CC, Jacobs DJ (2014) Principal component analysis: a method for determining the essential dynamics of proteins. Methods Mol Biol 1084:193–226

43. Jones KS, VanDongen HM, VanDongen AM (2002) The NMDA receptor M3 segment is a conserved transduction element coupling ligand binding to channel opening. J Neurosci 22(6):2044–2053

44. Twomey EC et al (2017) Channel opening and gating mechanism in AMPA-subtype glutamate receptors. Nature 549:60

45. Issack BB et al (2012) Exploring the essential collective dynamics of interacting proteins: application to prion protein dimers. Proteins 80(7):1847–1865

46. Hayward S, de Groot B (2008) *Normal modes and essential dynamics* 443:89–106

47. Wriggers W, Schulten K (1997) Protein domain movements: detection of rigid domains and visualization of hinges in comparisons of atomic coordinates. Proteins: Structure, Function, and Bioinformatics 29(1):1–14

48. Durham RJ et al (2020) Conformational spread and dynamics in allostery of NMDA receptors. Proc Natl Acad Sci U S A 117(7):3839–3847

49. Chang HR, Kuo CC (2008) The activation gate and gating mechanism of the NMDA receptor. J Neurosci 28(7):1546–1556

50. Sobolevsky AI, Beck C, Wollmuth LP (2002) Molecular rearrangements of the extracellular vestibule in NMDAR channels during gating. Neuron 33(1):75–85

51. Sobolevsky AI et al (2007) Subunit-specific contribution of pore-forming domains to NMDA receptor channel structure and gating. J Gen Physiol 129(6):509–525

52. Sobolevsky AI, Rooney L, Wollmuth LP (2002) Staggering of subunits in NMDAR channels. Biophys J 83(6):3304–3314

53. Sobolevsky AI, Yelshansky MV, Wollmuth LP (2003) Different gating mechanisms in glutamate receptor and K+ channels. J Neurosci 23(20):7559–7568

54. Sobolevsky AI, Yelshansky MV, Wollmuth LP (2004) The outer pore of the glutamate receptor channel has 2-fold rotational symmetry. Neuron 41(3):367–378

55. Talukder I, Borker P, Wollmuth LP (2010) Specific sites within the ligand-binding domain and ion channel linkers modulate NMDA receptor gating. J Neurosci 30(35):11792–11804

56. Cuello LG et al (2010) Structural basis for the coupling between activation and inactivation gates in K+ channels. Nature 466:272